Nanoscale

PAPER

View Article Online
View Journal | View Issue

Cite this: *Nanoscale*, 2017, **9**, 1237

Pine needle-derived microporous nitrogen-doped carbon frameworks exhibit high performances in electrocatalytic hydrogen evolution reaction and supercapacitors†

Guoyin Zhu,‡[a] Lianbo Ma,‡[a] Hongling Lv,[a] Yi Hu,[a] Tao Chen,[a] Renpeng Chen,[a] Jia Liang,[a] Xiao Wang,[a] Yanrong Wang,[a] Changzeng Yan,[a] Zuoxiu Tie,[a] Zhong Jin*[a] and Jie Liu*[a,b]

Received 17th October 2016,
Accepted 13th December 2016

DOI: 10.1039/c6nr08139h

www.rsc.org/nanoscale

The design of electrochemically active materials with appropriate structures and compositions is very important for applications in energy conversion and storage devices. Herein, we demonstrate an effective strategy to prepare microporous heteroatom-doped carbon frameworks derived from naturally-abundant pine needles. The preparation procedure is based on the carbonization of pine needles, followed by KOH activation at a temperature range of 700–1000 °C. The resultant nitrogen-doped carbon consists of abundant micropores and an ultrahigh specific surface area (up to 2433 $m^2 g^{-1}$), leading to high performances in electrocatalytic hydrogen evolution reaction (HER) and supercapacitors. Specifically, when the pine needle-derived carbon (activated at 800 °C) serves as a HER electrocatalyst, it exhibits a low onset potential (~4 mV), a small Tafel slope (~45.9 mV dec^{-1}) and a remarkable stability over long-term cycling. When evaluated as an electrode material for supercapacitors, the pine needle-derived carbon (activated at 900 °C) demonstrates high specific capacitance (236 F g^{-1} at 0.1 A g^{-1}), remarkable rate capability (183 F g^{-1} at even 20 A g^{-1}) and good long-term stability. Notably, the specific capacitance at 2.0 A g^{-1} increased from ~205 to ~227 F g^{-1} after cycling for 5000 times, owing to the further activation and wetting of the electrodes. This novel and low-cost biomass-derived carbon material is very promising for many applications, especially in electrocatalytic water splitting and supercapacitors.

Introduction

With the increasing global crisis of environmental pollution and energy problem, the development of novel technologies for clean and sustainable energy has attracted considerable attention.[1–3] In particular, hydrogen energy and supercapacitors have been regarded as "green" energy technologies because of their high efficiency and eco-friendliness.[4–7] However, there are still some critical issues restricting their development, such as slow kinetics and expensive electrocatalysts for the hydrogen evolution reaction (HER)[8,9] and low energy density for supercapacitors.[10,11]

Porous carbon materials possess many advantageous properties, such as large surface area, adjustable porosity, high electrical conductivity, versatile morphology, chemical inertness and abundant electrocatalytic active sites.[12,13] With these properties, porous carbon materials have become a class of promising candidates for the applications in oxygen reduction reaction[14,15] and supercapacitors.[16] Moreover, covalently-doped porous carbons with bound heteroatoms (*e.g.*, N, P and S) can show better wettability and enhanced performances.[17–19] Specifically, nitrogen-doped carbon materials were proved to be effective for energy conversion, such as the HER.[20] Besides, recently nitrogen-doped microporous carbon sheets have been reported to show good rate capability and high specific capacitance for supercapacitors.[21] Therefore, nitrogen-doped microporous carbons hold significant promise for energy conversion and storage applications. However, the structural design and controllable synthesis of heteroatom-doped carbon materials with a favorable pore size and a large pore volume is still challenging.

Recently, carbon-enriched biomass has become attractive precursors for the preparation of a variety of carbon

[a]*Key Laboratory of Mesoscopic Chemistry of MOE and Collaborative Innovation Center of Chemistry for Life Sciences, School of Chemistry and Chemical Engineering, Nanjing University, Nanjing, Jiangsu 210093, China. E-mail: zhongjin@nju.edu.cn, j.liu@duke.edu*

[b]*Department of Chemistry, Duke University, Durham, NC 27708, USA*

†Electronic supplementary information (ESI) available. See DOI: 10.1039/c6nr08139h

‡These authors contributed equally to this work.

materials.[22–28] In plant tissues, the transport channels of water and nutrients can provide diverse pore structures. Besides, since many kinds of biomass contain different doping elements, such as N, S, and P, it is convenient to prepare heteroatom-doped carbon materials through the controlled pyrolysis of biomass. Moreover, biomass-derived carbon materials are eco-friendly and can be produced on a large scale for practical applications. So far, many natural materials, such as coconut shells,[23] bamboo,[24] peanut root nodules,[25] silk,[26] leaves[27] and hairs,[28] *etc.*, have been widely used to prepare porous carbon. The biomass precursors greatly reduce the cost of production and also retain the structural diversity of source substances. In order to improve the performance of biomass-derived carbons obtained from thermal carbonization, further activation processes are usually required. Biomass-derived carbon materials with high porosity, good electrical conductivity and abundant heteroatom contents are particularly promising for the applications of energy devices.

Herein, we demonstrate an efficient strategy for the preparation of pine needle-derived microporous and nitrogen-doped carbon frameworks (PNCs) as an advanced electrode material for electrocatalytic HER and supercapacitors. Compared to other commonly-used biomass precursors, the natural abundance and the low cost of pine needles are very attractive. By temperature-controlled KOH activation of pre-carbonized pine needles, unique microporous carbons with adjustable pore structure, moderate nitrogen doping and high specific surface area were prepared. Owing to the well-designed nanoarchitecture, the PNCs activated at 800 °C exhibit remarkable HER activity with a low onset potential and long-term cycle life compared to existing carbonous materials reported in the literature (Table S1†).[25,29–35] Furthermore, the PNCs activated at 900 °C show large specific capacitance, great rate capability and high cycling stability over 5000 cycles in supercapacitors, superior or comparable to other biomass-derived carbons (Table S2†).[28,36–44] These results show the great potential of cheap and scalable PNCs for the applications in clean energy systems.

Experimental

Synthesis of PNCs

The dry pine needles (Asian Red Pine, *Pinus koraiensis Siebold et Zuccarini*) were collected from East China in May. All other chemicals were purchased from Sinopharm Chemical Reagent Co., Ltd and used as received without further treatment. The pine needles were firstly washed with deionized water several times to remove impurities and dried at 110 °C for 4 h. Then the pine needles were pre-carbonized at 600 °C for 1 h under an Ar atmosphere. The yield was approximately 40% after carbonization. The resultant was ball-milled by using a planetary ball miller (XGB2, Nanjing Boyuntong Corp.) with a 50 mL stainless steel tank and stainless steel beads at 500 rpm for 30 min. The product was mixed with KOH (weight ratio of KOH : carbon = 4 : 1) and pyrolyzed in a horizontal tube furnace under a N_2 flow of 50 mL min^{-1} and a heating ramp rate of 5 °C min^{-1} at 700, 800 or 900 °C for 1 h. The product was washed thoroughly with excess HCl solution (10 wt%) and deionized water, and finally dried overnight at 110 °C. The as-obtained PNC samples are termed PNC-*T*, where *T* is the temperature of activation. For comparison, two control samples were prepared by direct carbonization at the temperature of 800 °C and 900 °C without KOH activation, and termed d-PNC-800 and d-PNC-900, respectively.

Characterization

The samples were examined by scanning electron microscopy (SEM, HITACH S-4800), transmission electron microscopy (TEM, JEM-2100) and energy-dispersive X-ray spectroscopy (EDX) in conjunction with SEM. Powder X-ray diffraction (XRD) patterns were obtained with a Shimadzu XRD-6000 X-ray diffractometer equipped with a Cu Kα radiation source (λ = 1.54178 Å). Raman spectra were obtained using a JY LabRAM Evolution instrument with an excitation wavelength of 473 nm. Nitrogen adsorption–desorption isotherms were measured at 77 K using a Quantachrome Autosorb-IQ-2C analyzer at 77 K. The specific surface area was calculated by the Brunauer–Emmett–Teller (BET) method and pore size distribution was calculated from the desorption branch of the isotherms based on the Quenched Solid Density Functional Theory (QSDFT) model. X-ray photoelectron spectra (XPS) were obtained using a PHI-5000 VersaProbe X-ray photoelectron spectrometer with an excitation source of Al Kα X-ray radiation.

Measurements of electrocatalytic HER

Firstly, 980 μL of ethanol, 20 μL of Nafion (5 wt%) and 5 mg of the above mentioned PNC sample were mixed and sonicated for 1 h to form a homogeneous slurry. Then, 5 μL of the slurry was cast and dried on a freshly-polished glassy carbon electrode (GCE, 3 mm in diameter) as the working electrode. The Pt wire and the saturated calomel electrode (SCE) were used as the counter electrode and the reference electrode, respectively. The electrochemical measurements were carried out with a Chenhua CHI-760 electrochemical workstation. Linear sweep voltammetry (LSV) was carried out at a scan rate of 5 mV s^{-1} in 0.5 M H_2SO_4. The electrolyte was degassed by bubbling high-purity nitrogen to eliminate dissolved oxygen.

Measurements of supercapacitors

Supercapacitive performance of the samples was measured by using a two electrode system. Briefly, 80 wt% of the as-prepared PNC sample, 10 wt% of acetylene black and 10 wt% of PTFE binder (60 wt% dispersion in water) were homogeneously mixed and then cast onto a nickel foam (JYS01, Kunshan Jiayisheng) with a thickness of 3 mm as the current collector. The loading mass of the PNC sample was ~6 mg cm^{-2} on nickel foam. After drying under vacuum at 120 °C for 6 h, two PNC based electrodes were assembled in a CR2032 coin-type cell with a porous cellulose membrane as the separator and 6.0 M KOH as the electrolyte. Electrochemical impedance spectroscopy (EIS) was performed with an AC voltage

amplitude of 5 mV in a frequency range from 0.01 Hz to 100 kHz. The specific capacitance (C_s, F g^{-1}) of supercapacitors was calculated according to the following equation:

$$C_s = (2 \times I \times \Delta t)/(m \times \Delta V) \quad (1)$$

where I (A) represents the discharge current, m (g) is the loading mass of active materials on the electrode, Δt (s) is the discharge time and ΔV is the potential drop during discharge processes. Meanwhile, the energy density (E, Wh kg^{-1}) of supercapacitors was calculated by:

$$E = C_s \times V^2/(2 \times 4 \times 3.6) \quad (2)$$

where V is the voltage at the beginning of discharge steps. By dividing a factor of 3.6, the unit of E was converted from J g^{-1} to Wh kg^{-1}. The average power density (P, W kg^{-1}) was obtained by:

$$P = E \times 3600/\Delta t \quad (3)$$

Results and discussion

Preparation and characterization of PNCs

The schematic diagram for preparing PNCs through an effective thermal carbonization and activation approach is illustrated in Fig. 1a. A photograph of pine needles before collection is shown in Fig. 1b. The cleaned pine needles were pre-carbonized at 600 °C under an Ar atmosphere to obtain an intermediate carbonous product (inset in Fig. 1b). As shown in Fig. 1c, the pre-carbonized pine needles possess many tiny tubules with diameters of about 20–30 μm. After ball-milling and activation by KOH at 900 °C, the pine needles were turned into microporous carbon frameworks, termed PNC-900 (Fig. 1d and e). TEM characterization was also performed to investigate the morphological characteristics and nanostructures of PNC samples (Fig. 1f, g and S1†). All the samples exhibited a similar appearance and nanostructure compared to those of PNC-900. The carbon frameworks are composed of well-developed porous structures, providing favorable pathways for the diffusion and absorption of ions.

As shown in Fig. 2a, wide-angle X-ray diffraction (XRD) was employed to confirm the crystallographic structures of the as-prepared PNC materials. With the increase of carbonization temperature, the diffraction peak between 20 and 30° attributed to the (002) planes of graphitic carbon gradually shifted to higher angles. Furthermore, the increase of diffraction intensity at low scattering angles indicates the increased amount of micropores in the samples.[28,40,45,46] In the XRD patterns of PNC-700, PNC-800 and PNC-900, a weak peak emerges at approximately 43° which is attributed to the (100) planes of graphitic carbon, indicating a relatively low graphitization degree.[47] When the carbonization temperature reached 1000 °C, this peak is very minimal owing to the improved graphitization degree.

Raman spectra (Fig. 2b) of the samples show two obvious peaks around 1350 cm^{-1} and 1580 cm^{-1}, corresponding to the characteristic D (defects and disorder) and G (graphitic) bands of carbon materials, respectively. It is known that the ratio of band intensities (I_D/I_G) indicates the degree of structural disorder and defect intensity.[48] The I_D/I_G of PNC-700, PNC-800, and PNC-900 was measured to be 0.99, 0.96, and 0.94, respectively, reflecting the existence of abundant structural defects. However, the I_D/I_G of PNC-1000 sharply decreased to 0.45, suggesting a higher graphitization level.

The N_2 adsorption–desorption isotherms (Fig. 2c) of PNC-700, PNC-800, PNC-900, and PNC-1000 are typical type I curves, indicating the existence of a large amount of micropores. The abundant micropores are very beneficial for ion storage during charge–discharge processes.[49–51] The specific surface area of PNC-900 was found to be 2433 m^2 g^{-1}, higher than that of PNC-800 (1931 m^2 g^{-1}) and PNC-700 (985 m^2 g^{-1}). The specific surface area of PNC-1000 (2300 m^2 g^{-1}) is slightly lower than that of PNC-900, owing to the partial pore collapse

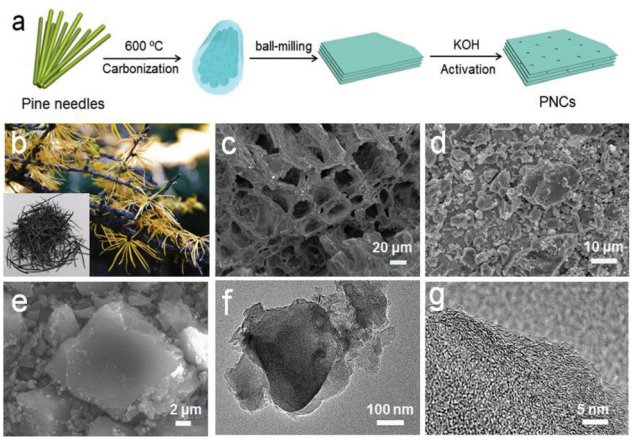

Fig. 1 (a) Schematic illustration of the synthesis process of PNCs. (b) Photo of raw pine needles. Inset in (b) shows a photo of pine needles after pre-carbonization at 600 °C. (c) Cross-section SEM image of pine needles after pre-carbonization at 600 °C. (d, e) SEM images of PNC-900. (f) TEM image of PNC-900. (g) HRTEM image of an edge area of PNC-900.

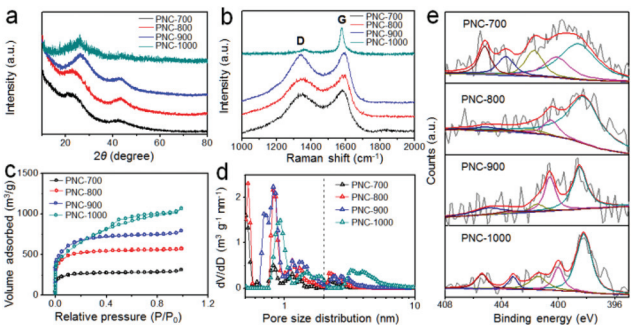

Fig. 2 (a) XRD patterns, (b) Raman spectra, (c) nitrogen adsorption–desorption isotherms, (d) pore size distributions and (e) XPS spectra of PNC-700, PNC-800, PNC-900 and PNC-1000 samples in N 1s region, respectively.

arising from higher carbonization temperature. All the N_2 adsorption–desorption isotherms show narrow knees, indicating the presence of narrow pore size distribution. The corresponding pore size distributions of the samples estimated by the QSDFT method (Fig. 2d) show the presence of micropores with the pore size between 0.5 and 2.0 nm, which is favorable for the formation of electrical double layers.[27] A small fraction of mesopores with diameters between 2.0 and 5.0 nm was also observed, which is beneficial to the ion diffusion and rate performance.

Biomass-derived carbon materials usually contain nitrogen heteroatoms originating from the $-NH_2$ groups.[52] In this study, the nitrogen element was found in all PNC materials by XPS analysis (Fig. 2e). The total content of nitrogen atoms in PNC-700 was measured to be 1.5 at%. With the increase of pyrolysis temperature, the N content of PNC-800, PNC-900 and PNC-1000 decreased to 1.4, 1.1 and 1.0 at%, respectively. In accordance with the literature,[53–55] five different forms of nitrogen species were found in PNC materials: pyridinic-N (N-6, 398.4 ± 0.2 eV), pyrrolic-N (N-5, 400.3 ± 0.2 eV), graphitic N (N-Q, 401.5 ± 0.2 eV), pyridine-N-oxide (N-4, 403.5 ± 0.2 eV) and N_2 (405.0 ± 0.1 eV).[56,57] The N-6 and N-5 species made a major contribution to create additional active sites for the enhancement of electrocatalytic activity towards the HER and the charge storage in supercapacitors.[30,53,58–60]

Performances of PNC based electrodes towards the HER

The electrocatalytic HER performances of PNC samples were examined in 0.50 M H_2SO_4 using a standard three-electrode system with a loading amount of 0.35 mg cm^{-2}. Fig. 3a shows the LSV polarization curves of PNC samples. For comparison, the HER performance of the d-PNC-800 control sample was also measured (Fig. 3a), showing a poor electrocatalytic activity compared to KOH-activated PNC samples. Among the PNC products, the onset overpotentials of PNC-800, PNC-900 and PNC-1000 are only −0.004 V, −0.004 V and −0.009 V, respectively, owing to their high catalytic activity and large surface area. Compared to other carbon-based materials or transition metal chalcogenides in the literature (Table S1†),[25,29–35] the PNC samples have much lower onset overpotentials. The overpotential (η) reflects the polarization degree upon the passage of Faradaic current (in this case due to H_2 evolution);[61] a lower η at the same potential suggests better catalytic activity for producing H_2. The η of PNC-800 at 10 mA cm^{-2} is −62 mV, much lower than that of PNC-700 (−116 mV), PNC-900 (−74 mV) and PNC-1000 (−120 mV), indicating the smooth electron transfer through the PNC-800 based electrode. The linear portions of Tafel plots were fitted well to the Tafel equation ($\eta = b(\log j) + a$), where j is the current density, and b is the Tafel slope. As shown in Fig. 3b, the Tafel slopes of PNC-700, PNC-800, PNC-900 and PNC-1000 are 71.2, 45.9, 64.3 and 79.9 mV dec^{-1}, respectively. These results also confirm that PNC-800 exhibits the best HER activity among all the samples. The high HER activity of PNC-800 could be attributed to the synergistic effect of the high nitrogen content and the high surface area, which may significantly enhance the HER activity by generating a large number of active sites and decreasing the adsorption free energy of the H atoms.[31,62] The catalytically-active surface area of carbon materials can be estimated by the capacitance of electrical double layers at the solid–liquid interface.[63] As shown in Fig. S2,† the double layer capacitance of PNC-800 was calculated to be 2.4 mF cm^{-2} (Fig. S2e†), much higher than those of PNC-700 (0.94 mF cm^{-2}), PNC-900 (1.1 mF cm^{-2}) and PNC-1000 (0.87 mF cm^{-2}), suggesting that PNC-800 possesses more active sites.

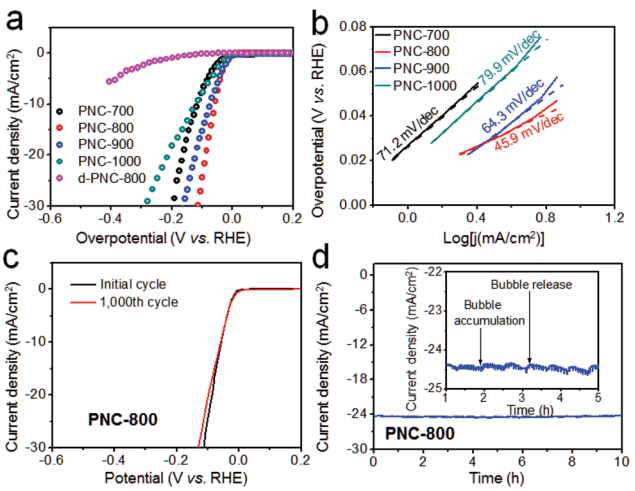

Fig. 3 (a) LSV curves and (b) corresponding Tafel plots of PNC samples for HER in 0.50 M H_2SO_4. (c) Polarization curves of PNC-800 recorded before and after 1000 potential sweeps (0.2 to −0.8 V *vs.* RHE) in 0.50 M H_2SO_4. (d) Time-dependent current density of the PNC-800 electrode at the potential of −0.1 V *vs.* RHE.

The long-term stability is an important parameter to evaluate the performance of electrocatalysts. The cycling stability of PNC-800 in acidic solution was studied by sweeping for 1000 cycles (Fig. 3c), showing only a slight decrease of cathodic currents. Furthermore, the practical long-term stability operating at a constant potential was also examined (Fig. 3d and S3†); the current values of all the samples remained almost constant at the overpotential of −0.1 V after cycling for 10 h. Small serrate fluctuations are observed in the inset of Fig. 3d, owing to the consumption of H^+ and the intermittent accumulation of H_2 bubbles.[29] Overall, PNC-800 shows the best electrocatalytic performance towards the HER among all the samples.

Performances of PNC based electrodes in supercapacitors

The supercapacitive performances of PNC based electrodes were evaluated by the measurements of two-electrode coin-type supercapacitors with 6.0 M KOH as the electrolyte. For comparison, the capacitive behavior of the d-PNC-900 control sample was also studied. Fig. 4a and S4† show the CV curves of d-PNC-900 and PNC based electrodes in a potential window of 0–1.0 V at different scan rates. The CV curve of d-PNC-900 shows very poor capacitive performance. In contrast, the quasi-rectangular-shaped CV curves of PNC samples indicate that the capacitances originate from the electrical double layers at

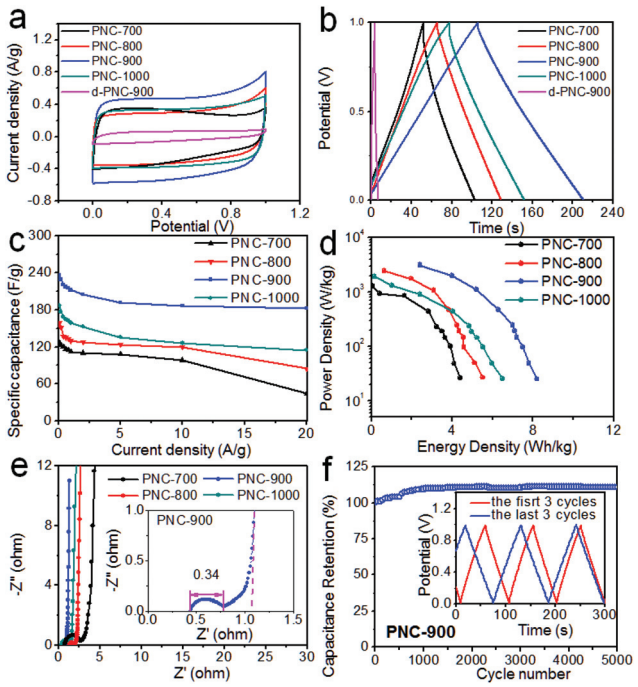

Fig. 4 (a) CV curves of PNC based electrodes at a scan rate of 5 mV s^{-1}. (b) Galvanostatic charge–discharge curves at a current density of 1.0 A g^{-1}. (c) Specific capacitances of PNC based electrodes as a function of charge–discharge current density. (d) Corresponding Ragone plots (specific energy *vs.* specific power) of PNC based supercapacitors. (e) Nyquist plots of PNC based electrodes in a frequency range of 0.01 Hz to 100 kHz. (f) Cycling stability of the PNC-900 based supercapacitor at a current density of 2.0 A g^{-1} for 5000 cycles. The inset shows the first and the last 3 cycles during the 5000 cycles of galvanostatic charge–discharge curves, indicating the increase of specific capacitance attributed to the further activation and wetting of PNC-900 based electrodes.

electrode–electrolyte interfaces. Among all the samples, PNC-900 exhibits the highest scanning current densities. The galvanostatic charge/discharge curves are depicted in Fig. 4b, where the samples were tested at 1.0 A g^{-1}. The specific capacitances were calculated to be 8, 112, 130, 212, and 159 F g^{-1} for d-PNC-900, PNC-700, PNC-800, PNC-900 and PNC-1000, respectively. It is clear that the electrochemical capacitances are remarkably improved by KOH activation at an appropriate temperature. Fig. S4† exhibits the galvanostatic charge–discharge curves of PNC based supercapacitors at different current densities, showing highly linear and nearly symmetric triangular characteristics that indicates good reversibility. Additionally, the low voltage drops reflect the small internal resistance of PNC based electrodes. The PNC-900 based electrode shows the longest discharging time compared to those of other electrodes at the same current densities, consistent with the CV results. Even at a high current density of 20 A g^{-1} (Fig. S5f†), PNC-900 based electrodes can also be charged/discharged smoothly with symmetric and linear lines, suggesting good capacitive performance and fast electron/ion transport.

The specific capacitances of PNC based electrodes calculated from galvanostatic charge–discharge curves are presented in Fig. 4c. At the current density of 0.1 A g^{-1}, PNC-900 shows the highest specific capacitance of 236 F g^{-1}. Even at a current density of 20 A g^{-1}, the specific capacitance of PNC-900 still remained at 183 F g^{-1} (with a retention of ~78%), reflecting an outstanding rate capability. This result can be ascribed to the relatively high graphitization degree that guarantees good electrical conductivity and also the nitrogen doping that improves the hydrophilicity for electrolyte transportation.[18,64] The Ragone plots (Fig. 4d) confirm that PNC-900 shows the best performance among all the samples. At the current density of 0.1 A g^{-1}, the specific energy density of the PNC-900 based supercapacitor is 8.2 Wh kg^{-1} (Fig. S6†), which is much larger than that of existing commercial supercapacitors (usually less than 4 Wh kg^{-1})[65] and previously-reported supercapacitors based on other N-doped porous carbon materials (typically 6.7 Wh kg^{-1}).[17,66–71] The area-normalized capacitance of PNC-900 (9.7 μF cm^{-2} at the current density of 0.1 A g^{-1}) is comparable with other previously-reported N-doped carbon materials (Table S3†).[17,72–76]

EIS measurements were also performed at the open circuit potential with an AC perturbation of 5 mV in the frequency range of 0.01 Hz to 100 kHz, as shown in Fig. 4e. The Nyquist plots of PNC samples show a vertical curve in the low-frequency region, confirming a nearly ideal capacitive behavior. By extrapolating the vertical portion of the plot to the real axis, the equivalent series resistance (ESR) of the PNC-900 based supercapacitor is measured to be 1.03 Ω. According to the diameter of the semicircle, PNC-900 also has very small charge transfer resistance of 0.34 Ω owing to its large ion-accessible surface area.[18]

Furthermore, the long-term cycling stability of the PNC-900 based supercapacitor was investigated by galvanostatic charge–discharge measurements between 0 and 1.0 V at the current density of 2.0 A g^{-1} for 5000 cycles (Fig. 4f). Notably, the specific capacitance gradually increased from 205 to ~226 F g^{-1} in the initial 1500 cycles, and then remained relatively stable and finally reached 227 F g^{-1} after 5000 cycles. This result can be ascribed to the further wetting and activation of the PNC material induced by ion intercalation/de-intercalation into and out of the micropores.[21,77] As shown in the insert of Fig. 4f, the increase of specific capacitance after long-term cycling is also evidenced by the galvanostatic charge–discharge curves of the initial 3 cycles and the last 3 cycles. Moreover, the galvanostatic charge–discharge curves still remain symmetric and undistorted after 5000 cycles, further suggesting the remarkable stability.

Conclusions

In this work, we report that pine needles can be used as a promising precursor material for the large-scale production of microporous N-doped carbon frameworks as a high-performance HER catalyst and a supercapacitor electrode material. With the highly-conductive microporous carbon scaffolds and heteroatom-induced active sites, the PNC material exhibits a

low onset potential, a small Tafel slope and long-term cycling stability towards the HER. Additionally, due to the high surface area and abundant micropores for charge storage and the nitrogen-substituted surface with high wettability, the PNC based supercapacitors present large specific capacitance, high rate performance and long cycling life. These results show the great potential of the PNC material in the applications of energy conversion and storage.

Acknowledgements

This work was supported by the National Materials Genome Project (2016YFB0700600), the National 973 Basic Research Program (2015CB659300), the National Natural Science Foundation of China (21403105 and 21573108), the China Postdoctoral Science Foundation (2015M580408, 2015M580413 and 2015M581768), the Natural Science Foundation for Young Scholars of Jiangsu Province (BK20150583, BK20150571 and BK20160647), the Fundamental Research Funds for the Central Universities and a project funded by the Priority Academic Program Development (PAPD) of Jiangsu Higher Education Institutions.

Notes and references

1 A. S. Arico, P. Bruce, B. Scrosati, J. M. Tarascon and W. Schalkwijk, *Nat. Mater.*, 2005, **4**, 366–377.
2 M. S. Dresselhaus and I. L. Thomas, *Nature*, 2001, **414**, 332–337.
3 X. Chen, C. Li, M. Grätzel, R. Kostecki and S. S. Mao, *Chem. Soc. Rev.*, 2012, **41**, 7909–7937.
4 J. A. Turner, *Science*, 2004, **305**, 972–974.
5 M. G. Walter, E. L. Warren, J. R. McKone, S. W. Boettcher, Q. Mi, E. A. Santori and N. S. Lewis, *Chem. Rev.*, 2010, **110**, 6446–6473.
6 G. Wang, L. Zhang and J. Zhang, *Chem. Soc. Rev.*, 2012, **41**, 797–828.
7 Y. Zhai, Y. Dou, D. Zhao, P. F. Fulvio, R. T. Mayes and S. Dai, *Adv. Mater.*, 2011, **23**, 4828–4850.
8 D. Merki and X. Hu, *Energy Environ. Sci.*, 2011, **4**, 3878–3888.
9 A. B. Laursen, S. Kegnæs, S. Dahl and I. Chorkendorff, *Energy Environ. Sci.*, 2012, **5**, 5577–5591.
10 P. Simon, Y. Gogotsi and B. Dunn, *Science*, 2014, **343**, 1210–1211.
11 C. Liu, F. Li, L. P. Ma and H. M. Cheng, *Adv. Mater.*, 2010, **22**, 28–62.
12 H. Nishihara and T. Kyotani, *Adv. Mater.*, 2012, **24**, 4473–4498.
13 L. L. Zhang and X. S. Zhao, *Chem. Soc. Rev.*, 2009, **38**, 2520–2531.
14 K. Gong, F. Du, Z. Xia, M. Durstock and L. Dai, *Science*, 2009, **323**, 760–764.
15 B. You, P. Yin and L. An, *Small*, 2014, **10**, 4352–4361.
16 T. Lin, I. W. Chen, F. Liu, C. Yang, H. Bi, F. Xu and F. Huang, *Science*, 2015, **350**, 1508–1513.
17 J. P. Paraknowitsch and A. Thomas, *Energy Environ. Sci.*, 2013, **6**, 2839–2855.
18 J. Zhao, H. Lai, Z. Lyu, Y. Jiang, K. Xie, X. Wang, Q. Wu, L. Yang, Z. Jin, Y. Ma, J. Liu and Z. Hu, *Adv. Mater.*, 2015, **27**, 3541–3545.
19 B. You, F. Kang, P. Yin and Q. Zhang, *Carbon*, 2016, **103**, 9–15.
20 Z. L. Wang, X. F. Hao, Z. Jiang, X. P. Sun, D. Xu, J. Wang, H. X. Zhong, F. L. Meng and X. B. Zhang, *J. Am. Chem. Soc.*, 2015, **137**, 15070–15073.
21 Z. Y. Jin, A. H. Lu, Y. Y. Xu, J. T. Zhang and W. C. Li, *Adv. Mater.*, 2014, **26**, 3700–3705.
22 B. Hu, K. Wang, L. Wu, S. H. Yu, M. Antonietti and M. M. Titirici, *Adv. Mater.*, 2010, **22**, 813–828.
23 D. Hulicova-Jurcakova, M. Seredych, G. Q. Lu and T. J. Bandosz, *Adv. Funct. Mater.*, 2009, **19**, 438–447.
24 W. Tian, Q. Gao, Y. Tan, K. Yang, L. Zhu, C. Yang and H. Zhang, *J. Mater. Chem. A*, 2015, **3**, 5656–5664.
25 Y. Zhou, Y. Leng, W. Zhou, J. Huang, M. Zhao, J. Zhan, C. Feng, Z. Tang, S. Chen and H. Liu, *Nano Energy*, 2015, **16**, 357–366.
26 J. Hou, C. Cao, F. Idrees and X. Ma, *ACS Nano*, 2015, **9**, 2556–2564.
27 M. Biswal, A. Banerjee, M. Deo and S. Ogale, *Energy Environ. Sci.*, 2013, **6**, 1249–1259.
28 W. Qian, F. Sun, Y. Xu, L. Qiu, C. Liu, S. Wang and F. Yan, *Energy Environ. Sci.*, 2014, **7**, 379–386.
29 Y. Zhao, F. Zhao, X. Wang, C. Xu, Z. Zhang, G. Shi and L. Qu, *Angew. Chem., Int. Ed.*, 2014, **53**, 13934–13939.
30 Y. Zheng, Y. Jiao, Y. Zhu, L. H. Li, Y. Han, Y. Chen, A. Du, M. Jaroniec and S. Z. Qiao, *Nat. Commun.*, 2014, **5**, 3783.
31 Y. Zheng, Y. Jiao, L. H. Li, T. Xing, Y. Chen, M. Jaroniec and S. Z. Qiao, *ACS Nano*, 2014, **8**, 5290–5296.
32 Y. Ito, W. Cong, T. Fujita, Z. Tang and M. Chen, *Angew. Chem., Int. Ed.*, 2015, **54**, 2131–2136.
33 Y. W. Tan, P. Liu, L. Y. Chen, W. T. Cong, Y. Ito, J. H. Han, X. W. Guo, Z. Tang, T. Fujita, A. Hirata and M. W. Chen, *Adv. Mater.*, 2014, **26**, 8023–8028.
34 J. Xie, H. Zhang, S. Li, R. Wang, X. Sun, M. Zhou, J. Zhou, X. W. Lou and Y. Xie, *Adv. Mater.*, 2013, **25**, 5807–5813.
35 M. S. Faber, R. Dziedzic, M. A. Lukowski, N. S. Kaiser, Q. Ding and S. Jin, *J. Am. Chem. Soc.*, 2014, **136**, 10053–10061.
36 M. Sevilla, W. Gu, C. Falco, M. M. Titirici, A. B. Fuertes and G. Yushin, *J. Power Sources*, 2014, **267**, 26–32.
37 G. Xu, J. Han, B. Ding, P. Nie, J. Pan, H. Dou, H. Li and X. Zhang, *Green Chem.*, 2015, **17**, 1668–1674.
38 J. Wang and Q. Liu, *RSC Adv.*, 2015, **5**, 4396–4403.
39 E. Raymundo-Piñero, F. Leroux and F. Béguin, *Adv. Mater.*, 2006, **18**, 1877–1882.
40 Y. S. Yun, S. Y. Cho, J. Shim, B. H. Kim, S. J. Chang, S. J. Baek, Y. S. Huh, Y. Tak, Y. W. Park, S. Park and H. J. Jin, *Adv. Mater.*, 2013, **25**, 1993–1998.
41 M. Genovese, J. Jiang, K. Lian and N. Holm, *J. Mater. Chem. A*, 2015, **3**, 2903–2913.

42 A. Ganesan, R. Mukherjee, J. Raj and M. M. Shaijumon, *J. Porous Mater.*, 2014, **21**, 839–847.
43 Z. Li, L. Zhang, B. S. Amirkhiz, X. Tan, Z. Xu, H. Wang, B. C. Olsen, C. M. B. Holt and D. Mitlin, *Adv. Energy Mater.*, 2012, **2**, 431–437.
44 P. Zhang, Z. Zhang, J. Chen and S. Dai, *Carbon*, 2015, **93**, 39–47.
45 W. Xing, J. S. Xue and J. R. Dahn, *J. Electrochem. Soc.*, 1996, **143**, 3046–3052.
46 L. Xie, G. Sun, F. Su, X. Guo, Q. Kong, X. Li, X. Huang, L. Wan, W. Song, K. Li, C. Lv and C. M. Chen, *J. Mater. Chem. A*, 2016, **4**, 1637–1646.
47 L. L. Zhang, H. H. Li, Y. H. Shi, C. Y. Fan, X. L. Wu, H. F. Wang, H. Z. Sun and J. P. Zhang, *ACS Appl. Mater. Interfaces*, 2016, **8**, 4233–4241.
48 C. Thomsen and S. Reich, *Phys. Rev. Lett.*, 2000, **85**, 5214–5217.
49 F. Béguin, V. Presser, A. Balducci and E. Frackowiak, *Adv. Mater.*, 2014, **26**, 2219–2251.
50 D. W. Wang, F. Li, M. Liu, G. Q. Lu and H. M. Cheng, *Angew. Chem.*, 2008, **120**, 379–382.
51 Y. Li, Z. Li and P. K. Shen, *Adv. Mater.*, 2013, **25**, 2474–2480.
52 Y. J. Kim, Y. Abe, T. Yanagiura, K. C. Park, M. Shimizu, T. Iwazaki, S. Nakagawa, M. Endo and M. S. Dresselhausd, *Carbon*, 2007, **45**, 2116–2125.
53 J. Zhang, Y. Cai, Q. Zhong, D. Lai and J. Yao, *Nanoscale*, 2015, **7**, 17791–17797.
54 Z. Li, L. Zhang, B. S. Amirkhiz, X. H. Tan, Z. W. Xu, H. L. Wang, B. C. Olsen, C. M. B. Holt and D. Mitlin, *Adv. Energy Mater.*, 2012, **2**, 431–437.
55 Y. Li, G. Wang, T. Wei, Z. Fan and P. Yan, *Nano Energy*, 2016, **19**, 165–175.
56 J. Zhang, G. Chen, Q. Zhang, F. Kang and B. You, *ACS Appl. Mater. Interfaces*, 2015, **7**, 12760–12766.
57 B. You, L. Wang, L. Yao and J. Yang, *Chem. Commun.*, 2013, **49**, 5016–5018.
58 H. Fei, Y. Yang, Z. Peng, G. Ruan, Q. Zhong, L. Li, E. L. G. Samuel and J. M. Tour, *ACS Appl. Mater. Interfaces*, 2015, **7**, 8083–8087.
59 Y. Liu, H. Yu, X. Quan, S. Chen, H. Zhao and Y. Zhang, *Sci. Rep.*, 2014, **4**, 6843.
60 L. Li, E. Liu, H. Shen, Y. Yang, Z. Huang, X. Xiang and Y. Tian, *J. Solid State Electrochem.*, 2011, **15**, 175–182.
61 M. Chhetri, S. Maitra, H. Chakraborty, U. V. Waghmare and C. N. R. Rao, *Energy Environ. Sci.*, 2016, **9**, 95–101.
62 J. Deng, P. Ren, D. Deng, L. Yu, F. Yang and X. Bao, *Energy Environ. Sci.*, 2014, **7**, 1919–1923.
63 D. Kong, H. Wang, Z. Lu and Y. Cui, *J. Am. Chem. Soc.*, 2014, **136**, 4897–4900.
64 Z. Li, Z. Xu, X. Tan, H. Wang, C. M. Holt, T. Stephenson, B. C. Olsen and D. Mitlin, *Energy Environ. Sci.*, 2013, **6**, 871–878.
65 Y. Gogotsi and P. Simon, *Science*, 2011, **334**, 917–918.
66 L. F. Chen, Z. H. Huang, H. W. Liang, H. L. Gao and S. H. Yu, *Adv. Funct. Mater.*, 2014, **24**, 5104–5111.
67 Y. Tan, C. Xu, G. Chen, Z. Liu, M. Ma, Q. Xie, N. Zheng and S. Yao, *ACS Appl. Mater. Interfaces*, 2013, **5**, 2241–2248.
68 H. Guo and Q. Gao, *J. Power Sources*, 2009, **186**, 551–556.
69 Z. S. Wu, A. Winter, L. Chen, Y. Sun, A. Turchanin, X. L. Feng and K. Müllen, *Adv. Mater.*, 2012, **24**, 5130–5135.
70 L. F. Chen, X. D. Zhang, H. W. Liang, M. Kong, Q. F. Guan, P. Chen, Z. Y. Wu and S. H. Yu, *ACS Nano*, 2012, **6**, 7092–7102.
71 L. Wang, G. Mu, C. Tian, L. Sun, W. Zhou, P. Yu, J. Yin and H. G. Fu, *ChemSusChem*, 2013, **6**, 880–889.
72 G. A. Ferrero, A. B. Fuertes and M. Sevilla, *J. Mater. Chem. A*, 2015, **3**, 2914–2923.
73 R. T. Wang, J. W. Lang and X. B. Yan, *Sci. China: Chem.*, 2014, **57**, 1570–1578.
74 H. Wang, Q. Gao, J. Hu and Z. Chen, *Carbon*, 2009, **47**, 2259–2268.
75 H. Wang, Z. Xu, A. Kohandehghan, Z. Li, K. Cui, X. Tan, T. J. Stephenson, C. K. King'ondu, C. M. B. Holt, B. C. Olsen, J. K. Tak, D. Harfield, A. O. Anyia and D. Mitlin, *ACS Nano*, 2013, **7**, 5131–5141.
76 L. Wei, M. Sevilla, A. B. Fuertes, R. Mokaya and G. Yushin, *Adv. Funct. Mater.*, 2012, **22**, 827–834.
77 X. Lu, D. Zheng, T. Zhai, Z. Liu, Y. Huang, S. Xie and Y. Tong, *Energy Environ. Sci.*, 2011, **4**, 2915–2921.